Reproducibility and Gap Control of Superconducting Flux Qubits

T. Chang,[1] I. Holzman,[1] T. Cohen,[1] B. C. Johnson,[2] D. N. Jamieson,[2] and M. Stern[1,*]

[1] *Quantum Nanoelectronics Laboratory, Department of Physics & Bar-Ilan Institute of Nanotechnology and Advanced Materials (BINA), Ramat-Gan 5290002, Israel*

[2] *ARC Centre for Quantum Computation and Communication Technology (CQC2T) & School of Physics, University of Melbourne, Parkville, VIC 3010, Australia*

(Received 3 July 2022; revised 28 September 2022; accepted 15 November 2022; published 20 December 2022)

Superconducting flux qubits are promising candidates for the physical realization of a scalable quantum processor. Indeed, these circuits may have both a small decoherence rate and a large anharmonicity. These properties enable the application of fast quantum gates with high fidelity and reduce scaling limitations due to frequency crowding. The major difficulty of flux qubits' design consists of controlling precisely their transition energy—the so-called qubit gap—while keeping long and reproducible relaxation times. Solving this problem is challenging and requires extremely good control of e-beam lithography, oxidation parameters of the junctions, and sample surface. Here we present measurements of a large batch of flux qubits and demonstrate a high level of reproducibility and control of qubit gaps (± 0.6 GHz), relaxation times (15–20 μs), and pure echo dephasing times (15–30 μs). These results open the way for potential applications in the fields of quantum hybrid circuits and quantum computation.

DOI: 10.1103/PhysRevApplied.18.064062

I. INTRODUCTION

Because of their long coherence times and ease of use [1–3], transmon qubits are today one of the most popular architectures for building superconducting quantum processors [4]. Yet, as one scales up the system, the large eigenvalue manifold of each transmon generates issues related to frequency crowding and gate fidelity [5]. In contrast to transmons, superconducting flux qubits [6–9] intrinsically possess a huge anharmonicity: the higher energy levels of the system are very far from the qubit transition. Consequently, the flux qubit behaves as a *true* two-level system, which limits frequency crowding problems. Moreover, it can be manipulated on a much shorter timescale (< 10 ns) and therefore could potentially exhibit better gate fidelity. In addition, this architecture offers interesting prospects for the development of hybrid quantum circuits since its large magnetic dipole could allow for an efficient transfer of quantum information between isolated quantum systems, such as spins in semiconductors [10–12].

The two major issues of flux qubit designs are device-to-device gap reproducibility and coherence [13–16]. The flux qubit transition energy—the so-called qubit gap—is difficult to control and requires an extremely precise tuning of the fabrication parameters. Moreover, the flux qubit coherence times are known for their sizeable irreproducibility. Long coherence times reported in previous works relate only to a few singular flux qubits [16]. In the last few years, flux qubits embedded in three dimensional (3D) cavities [17] or in coplanar resonators [18] have exhibited more reproducible and generally improved relaxation times. More recently, a design—the so-called capacitively shunted flux qubit—has shown even better coherence times [19]. However, this same shunting capacitance used to better control the qubit strongly decreases its anharmonicity. Clearly, further improvements in coherence times and in control are necessary if the flux qubit is to be an alternative option for quantum computation.

In this work, we present a good improvement in the control and reproducibility of these qubits. We present a systematical study of a large batch of more than 20 devices and demonstrate that it is possible to control their gap energy to within less than 1 GHz while obtaining reproducible relaxation times $T_1 \sim 15$–20 μs and pure dephasing times $T_{2E}^{\phi} \sim 15$–30 μs. This reproducibility enables us to analyze the different factors that impede the coherence times and systematically eliminate them. Our work opens perspectives for potential applications in the fields of quantum hybrid circuits and quantum computation.

II. CIRCUIT IMPLEMENTATION

Our method explores the role of the substrate in device variability by employing a standard gate oxide process based on other applications of CMOS device technology [20]. The three samples presented in this work are

*michael.stern@biu.ac.il

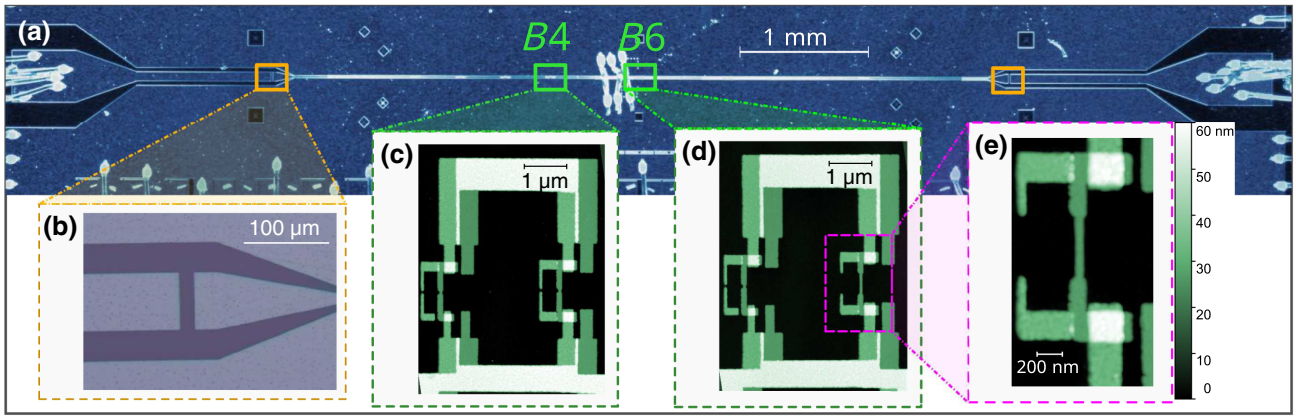

FIG. 1. Circuit implementation. (a) Optical microscope image of a $\lambda/2$ CPW resonator (resonator B) intersected and galvanically coupled to a series of 11 flux qubits labeled $B1$ to $B11$. The length of resonator B is 5.73 mm, such that the first resonant mode is at $f_{rB} \simeq 9.8$ GHz. (b) Enlarged view of the coupling capacitor terminating at both ends of the CPW resonator. The value of the capacitance is calculated by an electromagnetic simulator (Sonnet) to be $C_C \sim 5.0$ fF. (c) Colored AFM micrograph of qubit $B4$. The surface area of the large unitary junctions is $A_{\text{uni}} = 0.0526 \pm 0.0008\ \mu\text{m}^2$ and the small junction is chosen to have $\alpha = 0.5$. (d) Colored AFM micrograph of qubit $B6$. The surface area of the large unitary junctions and the ratio α are identical to those of $B4$. The loop of this qubit includes a thin constriction. (e) Enlarged view of the 30-nm-width constriction of qubit $B6$.

fabricated on silicon chips and contain a 150-nm-thick aluminum coplanar waveguide (CPW) resonator, with two symmetric ports used for microwave transmission measurements [see Fig. 1(a)]. The CPW resonator A is directly fabricated on a high-resistivity ($> 10\ \text{k}\Omega$ cm) silicon wafer with native oxide while resonators B and C are fabricated on a 5-nm thermally grown silicon oxide layer. A series of 11 flux qubits is galvanically coupled to each CPW resonator. In the following, the qubits are labeled according to their spatial position on the relevant resonator (e.g., $A1 \ldots A11, B1 \ldots B11, C1 \ldots C11$).

Our flux qubit design consists of a superconducting loop intersected by four Josephson junctions, one of which is smaller than the others by a factor α. This circuit behaves as a two-level system when the flux threading the loop is close to half a flux quantum $\Phi \sim \Phi_0/2$ [6,7]. Each level is characterized by the direction of a macroscopic persistent current I_P flowing in the loop of the qubit. The value of the persistent current I_P, typically of the order of 200–300 nA, gives rise to a huge magnetic moment (approximately 500 GHz/G), making the energy of each level very sensitive to external magnetic flux. At $\Phi = \Phi_0/2$, the two levels are degenerate, hybridize, and give rise to an energy splitting $h\Delta$ called the flux-qubit gap. At this point, the qubit is immune to flux noise at first order and should exhibit a long coherence time.

Figures 1(c) and 1(d) present atomic force microscope (AFM) images of qubits $B4$ and $B6$. The loop area of qubit $B4$ ($B6$) is $S_{B4} \simeq 13.3\ \mu\text{m}^2$ ($S_{B6} \simeq 12.4\ \mu\text{m}^2$). The three identical junctions have a Josephson energy $E_J/h = 360$ GHz and a single electron charging energy $E_C/h = 3.68$ GHz while the fourth junction is smaller than the others by $\alpha = 0.5$. In addition, qubit $B6$ contains a 30-nm-width constriction over a length of 500 nm [see Fig. 1(e)]. The qubits are fabricated by e-beam lithography with a trilayer CSAR-Ge-MAA process (see Supplemental Material [21] for more details). The germanium mask is rigid and robust to the oxygen ashing cleaning step. Moreover, it dissipates efficiently the charges during e-beam lithography and thus provides excellent precision and reproducibility of the junction sizes. The electron-beam lithography is followed by double-angle evaporation of Al-AlOx-Al performed at a well-controlled temperature ($-50\,^\circ\text{C}/+7\,^\circ\text{C}$). The low temperature enables us to reduce the grain size of aluminum, to better control the dimensions and oxidation of our junctions and to fabricate small constrictions with high fidelity.

III. SPECTROSCOPY AND COHERENCE PROPERTIES

We first characterize the qubit-resonator system by spectroscopic measurements (see Supplemental Material [21] for the experimental setup). Figures 2(a) and 2(b) show a continuous-wave transmission scan of resonator B taken as a function of the applied magnetic field. This measurement is performed with a vanishing power corresponding to an average of less than one photon in the resonator. We observe an anticrossing each time a qubit and the resonator are resonant. Far from the anticrossings, the resonance corresponding to the first mode of the resonator is $f_{rB} = 9.804$ GHz and its quality factor is $Q_B = 2800$ [21].

The frequency dependence of qubits $B4$ and $B6$ on Φ is shown in Figs. 2(c) and 2(d), respectively. The transition frequency of each qubit follows $f_{01} = \sqrt{\Delta^2 + \varepsilon^2}$ with $\varepsilon = 2I_P\,(\Phi - \Phi_0/2)\,/h$, yielding $\Delta^{(B4)} = 5.182$ GHz

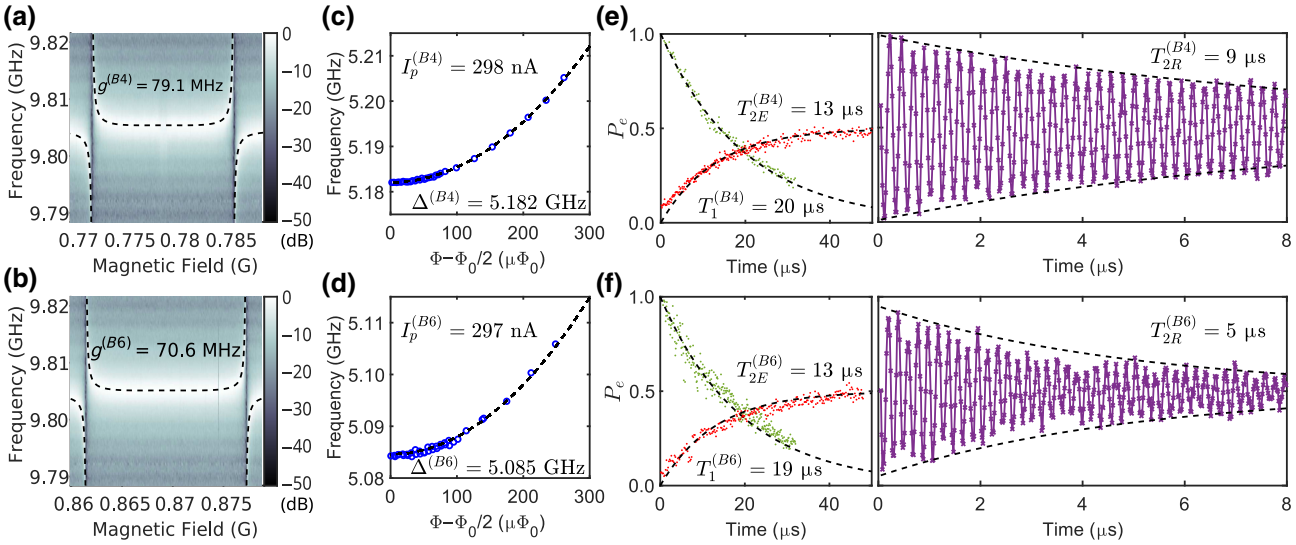

FIG. 2. Characterization of qubits $B4$ (top panels) and $B6$ (bottom panels). (a),(b) Transmission spectrum of CPW resonator B versus applied magnetic field showing anticrossing of qubit $B4/B6$. For each qubit we fit the anticrossing to our qubit-resonator coupling model and extract the value of the coupling constant g of the qubit with the resonator. (c),(d) Measured qubit frequency (blue circles) and fit (black dashed curve) yielding the qubit parameters Δ and I_p. (e),(f) Left panels: qubit energy relaxation and spin-echo measurements. The excited state probability P_e is plotted as a function of the delay between the π pulse and the readout pulse (green dots) or between the two $\pi/2$ pulses of the echo sequence (red dots). The black dashed line is an exponential fit to the energy relaxation (spin-echo) data. Right panels: measured Ramsey fringes (purple solid line) with fit to the exponentially decaying envelope.

and $I_P^{(B4)} = 298$ nA ($\Delta^{(B6)} = 5.085$ GHz, $I_P^{(B6)} = 297$ nA). Since both qubits are designed to have the same parameters, this seems to indicate excellent reproducibility of our e-beam lithography and oxidation parameters. Taking into account the contribution of geometric capacitance between neighboring islands allows us to fit the parameters of the flux qubits in good agreement with the measured values of α and E_J extracted from the Ambegaokar-Baratoff formula (see Supplemental Material [21]). We now turn to the coherence times at the so-called optimal point where the qubit frequency $f_{01} = \Delta$ is insensitive to first order to flux noise [13,14]. Energy relaxation decay is shown in Figs. 2(e) and 2(f) to be exponential for both qubits, with $T_1 = 20$ µs for $B4$ and 19 µs for $B6$. Ramsey fringes show an exponential decay for $B4$ with $T_{2R} = 9$ µs and for $B6$ with $T_{2R} = 5$ µs. Spin echo decays exponentially with identical dephasing times $T_{2E} = 13$ µs. Apparently, the presence of the constriction in qubit $B6$ does not seem to influence the coherence time of the qubit. This property is particularly exciting if one wishes to coherently couple a single spin to this circuit [12].

IV. REPRODUCIBILITY AND CONTROL

We repeat this procedure for the qubits of our three samples. Each qubit is thus characterized by its spectroscopic parameters Δ and I_P, extracted from the dependence of its transition frequency on the applied flux. In Fig. 3(a), we present a graph showing the gaps Δ of the different qubits versus their persistent currents I_P. In order to optimize our qubit design, we vary the size of the large unitary junctions of samples A, B, and C while keeping an approximately constant critical current density of approximately 13.5 µA µm^{-2}. Within each sample, the qubit parameters (E_J, E_C, α) are designed to be identical and thus the qubits should be clustered within a well-defined region. The extent of this region indicates the level of reproducibility of our fabrication process. A slight improvement in the data spread is observed for samples B and C in comparison with sample A. Quantitatively speaking, the gap average values are 6.9 ± 1, 5.1 ± 0.7, and 6.6 ± 0.6 GHz for samples A, B, and C, respectively. A principal component analysis (PCA) is performed on the covariance matrix of the (Δ, I_P) data points in order to define regions with high probability of finding a qubit. For each sample, a dashed line is presented and corresponds to the result of qubit numerical diagonalizations (see Supplemental Material [21]) while varying the parameter α by $\pm 5\%$ around their respective average value $\left(\langle E_J\rangle_{A/B/C}, \langle E_c\rangle_{A/B/C}, \langle\alpha\rangle_{A/B/C}\right)$. For the three samples, the principal axis and the numerical diagonalizations are well aligned indicating that the main origin of disorder is indeed uncontrolled variations of the value of the parameter α. The variation of the critical current density of the junctions due to different oxidation of samples A, B, and C ($\pm 5\%$) leads to an additional uncertainty of ± 150 MHz in the control of the desired qubit gap.

In Fig. 3(b), we present the spread of the relaxation rates Γ_1 of the different qubits. Qubit $A9$ exhibits the longest

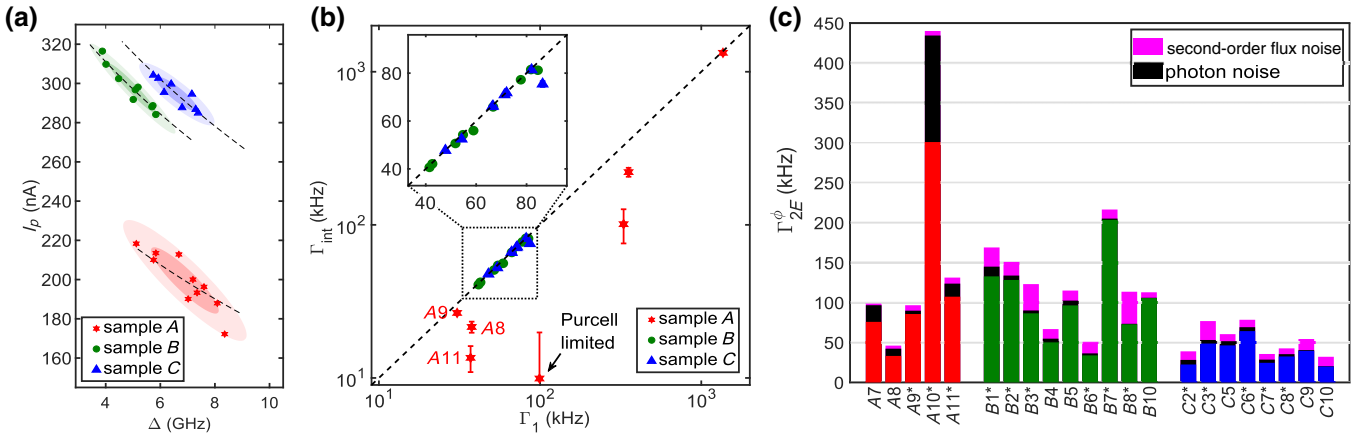

FIG. 3. Reproducibility and control. (a) Persistent current I_P versus gap Δ of the qubits of sample A (native oxide, red stars), sample B (5-nm-grown silicon oxide layer, green circles), and sample C (5-nm-grown silicon oxide layer, blue triangles). The colored regions are obtained by assuming a normal distribution along axes defined by PCA. The probability of finding a qubit within the dark (light) colored area is 50% (90%). The dashed black lines are obtained by numerical simulations of the flux qubits (see Supplemental Material [21]) at their average value $\left(\langle E_J\rangle_{A/B/C}, \langle E_c\rangle_{A/B/C}, \langle\alpha\rangle_{A/B/C}\right)$ while varying the parameter α by $\pm 5\%$. (b) The estimated intrinsic relaxation rates $\Gamma_{\rm int} = \Gamma_1 - \Gamma_P$ versus measured relaxation rates Γ_1 for qubits of samples A (red stars), B (green circles), and C (blue triangles). Errors due to calibration of the incoming power at the resonator input (± 1.5 dB) lead to uncertainties of a factor of 2 in the Purcell relaxation rate. (c) Stacked bar chart showing the pure dephasing rates Γ_{2E}^{ϕ} at optimal points of the measured qubits of samples A (red), B (green), and C (blue). The black color corresponds to the calculated decoherence rate due to photon noise in the first three modes of the resonator. The pink color corresponds to calculated decoherence rate due to second-order flux noise. The black stars indicate the presence of a 30-nm-width constriction in the loop of the qubit. The presence of a constriction does not seem to affect significantly the relaxation or the dephasing of the qubits.

relaxation time with $T_1 = 32\ \mu$s. Several mechanisms contribute to relaxation of qubits; among them is spontaneous emission by the qubit to the resonator (the so-called Purcell effect [22]). The Purcell rate Γ_P can be quantitatively determined by measuring the qubit Rabi frequency Ω_R for a given microwave power $P_{\rm in}$ at the resonator input. For a qubit coupled symmetrically to the input and output lines, a simple expression for Γ_P was obtained in Ref. [17]. We thus calculate Γ_P for each qubit and represent the intrinsic relaxation rates of the qubits defined as $\Gamma_{\rm int} = \Gamma_1 - \Gamma_P$. The average values of the intrinsic relaxation rates are 260 ± 440, 61 ± 15, and 68 ± 11 kHz for samples A, B, and C, respectively. These average numbers are comparable to those obtained in Ref. [19] for capacitively shunted flux qubits. Relaxation due to $1/f^{\gamma}$ flux noise can be safely neglected for qubits in our frequency range [19]. The spread of the relaxation rates in samples B and C is remarkable compared with sample A and more generally with the state of the art [17,18]. We thus come to the conclusion that better qubit reproducibility in terms of relaxation rates is obtained for samples with a thermally grown 5-nm-width silicon oxide layer. It is yet important to stress that the best relaxation rates (approximately 25 kHz) are obtained on intrinsic silicon (e.g., $A11$, $A8$). These findings are consistent with previous studies comparing loss tangents for silicon oxide and silicon at low temperatures [23–25]. Yet, the high variability of the devices on native oxide points toward an extreme sensitivity of the dielectric losses to the nanoscale variations in the stoichiometry and thickness of the oxide.

V. ORIGIN OF DEPHASING

In the rest of the paper, we focus on the origin of the dephasing rates of the qubits. Indeed, the noticeable reproducibility of the qubits enables us to analyze the different noise sources that influence the coherence times and systematically eliminate possible noise factors. We begin this analysis away from the optimal point, where the flux qubit decoherence is dominated by flux noise. The power spectrum of flux noise has a $1/f$ shape $S_\Phi[f] = A_\Phi^2/f$ [13,16–18]. Thus, measuring the flux qubit decoherence versus ε gives us direct access to the flux noise amplitude A_Φ [26,27]. Interestingly, we obtain almost the same flux noise amplitude $A_\Phi = 1.2 \pm 0.2\ \mu\Phi_0$ for all the qubits whether on sample A, B, or C including those with constrictions or not (see Supplemental Material [21]).

In Fig. 3(c), we show the pure echo dephasing rate $\Gamma_{2E}^{\phi} = \Gamma_{2E} - \Gamma_1/2$ at the optimal point for the different qubits. At this point, the qubits are protected against flux noise at first order. Yet, second-order effects may still impact the dephasing rates. To account for these effects, we perform a numerical Monte Carlo simulation detailed in the Supplemental Material [21]. At the optimal point, a

simple formula is obtained:

$$\Gamma_{2E}^{\text{opti}} \simeq 56\frac{(I_p A_\Phi/h)^2}{\Delta}.$$

The results of our analysis show that second-order flux noise can only explain partially the observed dephasing at the optimal point. Other well-known mechanisms of dephasing are related to photon noise in the resonator [13,19] and charge noise [17]. As shown in Fig. 3(c), photon noise has some impact on several qubits whose resonance happens to be close to that of the resonator. The sensitivity of flux qubits to charge noise is highly dependent on the ratio between the Josephson energy E_J and the charging energy E_C. We thus calculate the maximum amplitude of the charge modulation for each qubit (see Supplemental Material [21]). On average, the charge modulation is equal to 100, 5, and 1 kHz for samples A, B, and C, respectively. Clearly, this is more than 1 order of magnitude smaller than the measured pure dephasing rate for samples B and C and cannot explain the data. Thus, another mechanism is necessary to explain at least qualitatively the remaining dephasing rate of these qubits. Critical current fluctuations are for instance a possible channel of dephasing in our system. These fluctuations are due to charges localized in the barrier of the Josephson junctions. They also produce a $1/f$ shape spectral density [28,29]. Assuming that the remaining dephasing rate of sample C is fully due to this microscopic source of noise, we get $S_{I_0}[1\text{ Hz}] \simeq (0.5\text{ pA})^2\ \mu\text{m}^{-2}$, which seems compatible with previously reported values in the literature.

VI. CONCLUSION

In conclusion, we show that flux qubits can be fabricated in a reproducible way both in terms of gap transition energy and in terms of decoherence rates. Reproducible relaxation times are measured with $T_1 \sim 15$–$20\ \mu$s for samples fabricated on a thermally grown 5-nm SiO_2 layer. These numbers are comparable with those observed in Refs. [19,30] for capacitively shunted flux qubits. The major advantages of our design are its large anharmonicity ($f_{12} \sim 30$ GHz) and high persistent current ($I_p \sim 300$ nA). This makes flux qubits ideal candidates for magnetic coupling to spins such as N-V centers [10,12] or other impurities in silicon [31]. In all the samples, the amplitude of flux noise is low and reproducible $A_\phi = 1.2 \pm 0.2\ \mu\Phi_0$. At the optimal point, long and reproducible pure dephasing times are measured with $T_{2E}^{\phi} = 15$–$30\ \mu$s. At this level, the pure dephasing times are most likely limited by critical current fluctuations of the small junction of the qubits. Our results prove that flux qubits can reliably reach long coherence times and open interesting perspectives for both hybrid quantum circuits and scalable quantum processing.

ACKNOWLEDGMENTS

This research is supported by the Israeli Science Foundation under Grants No. 426/15, No. 898/19, and No. 963/19. We acknowledge the ARC Centre of Excellence for Quantum Computation and Communication Technology (CE170100012). M.S. wishes to acknowledge fruitful discussions with I. Bar Joseph, Y. Kubo, and G. Catelani.

[1] H. Paik, D. I. Schuster, L. S. Bishop, G. Kirchmair, G. Catelani, A. P. Sears, B. R. Johnson, M. J. Reagor, L. Frunzio, L. I. Glazman, S. M. Girvin, M. H. Devoret, and R. J. Schoelkopf, Observation of High Coherence in JoJephson junction Qubits Measured in a Three-Dimensional Circuit QED Architecture, Phys. Rev. Lett. **107**, 240501 (2011).

[2] A. P. M. Place *et al.*, New material platform for superconducting transmon qubits with coherence times exceeding 0.3 milliseconds, Nat. Commun. **12**, 1779 (2021).

[3] R. Barends, J. Kelly, A. Megrant, D. Sank, E. Jeffrey, Y. Chen, Y. Yin, B. Chiaro, J. Mutus, C. Neill, P. O'Malley, P. Roushan, J. Wenner, T. C. White, A. N. Cleland, and J. M. Martinis, Coherent Josephson Qubit Suitable for Scalable Quantum Integrated Circuits, Phys. Rev. Lett. **111**, 080502 (2013).

[4] F. Arute *et al.*, Quantum supremacy using a programmable superconducting processor, Nature **574**, 505 (2019).

[5] S. A. Caldwell *et al.*, Parametrically Activated Entangling Gates Using Transmon Qubits, Phys. Rev. Appl. **10**, 034050 (2018).

[6] J. E. Mooij, T. P. Orlando, L. Levitov, L. Tian, C. H. van der Wal, and S. Lloyd, Josephson persistent-current qubit, Science **285**, 1036 (1999).

[7] T. P. Orlando, J. E. Mooij, L. Tian, C. H. van der Wal, L. S. Levitov, S. Lloyd, and J. J. Mazo, Superconducting persistent-current qubit, Phys. Rev. B **60**, 15398 (1999).

[8] C. H. van der Wal, A. C. J. ter Haar, F. K. Wilhelm, R. N. Schouten, C. J. P. M. Harmans, T. P. Orlando, S. Lloyd, and J. E. Mooij, Quantum superposition of macroscopic persistent-current states, Science **290**, 773 (2000).

[9] I. Chiorescu, Y. Nakamura, C. J. P. M. Harmans, and J. E. Mooij, Coherent quantum dynamics of a superconducting flux qubit, Science **299**, 1869 (2003).

[10] D. Marcos, M. Wubs, J. M. Taylor, R. Aguado, M. D. Lukin, and A. S. Sørensen, Coupling Nitrogen-Vacancy Centers in Diamond to Superconducting Flux Qubits, Phys. Rev. Lett. **105**, 210501 (2010).

[11] J. Twamley and S. D. Barrett, Superconducting cavity bus for single nitrogen-vacancy defect centers in diamond, Phys. Rev. B **81**, 241202 (2010).

[12] T. Douce, M. Stern, N. Zagury, P. Bertet, and P. Milman, Coupling a single nitrogen-vacancy center to a superconducting flux qubit in the far-off-resonance regime, Phys. Rev. A **92**, 052335 (2015).

[13] P. Bertet, I. Chiorescu, G. Burkard, K. Semba, C. J. P. M. Harmans, D. P. DiVincenzo, and J. E. Mooij, Dephasing of a Superconducting Qubit Induced by Photon Noise, Phys. Rev. Lett. **95**, 257002 (2005).

[14] F. Yoshihara, K. Harrabi, A. O. Niskanen, Y. Nakamura, and J. S. Tsai, Decoherence of Flux Qubits due to $1/f$ Flux Noise, Phys. Rev. Lett. **97**, 167001 (2006).

[15] P. Forn-Díaz, J. Lisenfeld, D. Marcos, J. J. García-Ripoll, E. Solano, C. J. P. M. Harmans, and J. E. Mooij, Observation of the Bloch-Siegert Shift in a Qubit-Oscillator System in the Ultrastrong Coupling Regime, Phys. Rev. Lett. **105**, 237001 (2010).

[16] J. Bylander, S. Gustavsson, F. Yan, F. Yoshihara, K. Harrabi, G. Fitch, D. G. Cory, Y. Nakamura, J.-S. Tsai, and W. D. Oliver, Noise spectroscopy through dynamical decoupling with a superconducting flux qubit, Nat. Phys. **7**, 565 (2011).

[17] M. Stern, G. Catelani, Y. Kubo, C. Grezes, A. Bienfait, D. Vion, D. Esteve, and P. Bertet, Flux Qubits with Long Coherence Times for Hybrid Quantum Circuits, Phys. Rev. Lett. **113**, 123601 (2014).

[18] J.-L. Orgiazzi, C. Deng, D. Layden, R. Marchildon, F. Kitapli, F. Shen, M. Bal, F. R. Ong, and A. Lupascu, Flux qubits in a planar circuit quantum electrodynamics architecture: Quantum control and decoherence, Phys. Rev. B **93**, 104518 (2016).

[19] F. Yan, S. Gustavsson, A. Kamal, J. Birenbaum, A. P. Sears, D. Hover, T. J. Gudmundsen, D. Rosenberg, G. Samach, S. Weber, J. L. Yoder, T. P. Orlando, J. Clarke, A. J. Kerman, and W. D. Oliver, The flux qubit revisited to enhance coherence and reproducibility, Nat. Commun. **7**, 12964 (2016).

[20] J. J. Pla, K. Y. Tan, J. P. Dehollain, W. H. Lim, J. J. L. Morton, D. N. Jamieson, A. S. Dzurak, and A. Morello, A single-atom electron spin qubit in silicon, Nature **489**, 541 (2012).

[21] See Supplemental Material at http://link.aps.org/supplemental/10.1103/PhysRevApplied.18.064062 for a description of the experimental setup, the flux qubit model, derivation of the flux noise decoherence rates, derivation of the relationship between the Purcell rate and the Rabi oscillation and driving power, the qubit and resonator design parameters, the fabrication steps, and room-temperature characterization of junctions.

[22] A. A. Houck, J. A. Schreier, B. R. Johnson, J. M. Chow, J. Koch, J. M. Gambetta, D. I. Schuster, L. Frunzio, M. H. Devoret, S. M. Girvin, and R. J. Schoelkopf, Controlling the Spontaneous Emission of a Superconducting Transmon Qubit, Phys. Rev. Lett. **101**, 080502 (2008).

[23] J. M. Martinis, K. B. Cooper, R. McDermott, M. Steffen, M. Ansmann, K. D. Osborn, K. Cicak, S. Oh, D. P. Pappas, R. W. Simmonds, and C. C. Yu, Decoherence in Josephson Qubits from Dielectric Loss, Phys. Rev. Lett. **95**, 210503 (2005).

[24] J. Krupka, J. Breeze, A. Centeno, N. Alford, T. Claussen, and L. Jensen, Measurements of permittivity, dielectric loss tangent, and resistivity of float-zone silicon at microwave frequencies, IEEE Trans. Microw. Theory Tech. **54**, 3995 (2006).

[25] A. D. O'Connell, M. Ansmann, R. C. Bialczak, M. Hofheinz, N. Katz, E. Lucero, C. McKenney, M. Neeley, H. Wang, E. M. Weig, A. N. Cleland, and J. M. Martinis, Microwave dielectric loss at single photon energies and millikelvin temperatures, Appl. Phys. Lett. **92**, 112903 (2008).

[26] G. Ithier, E. Collin, P. Joyez, P. J. Meeson, D. Vion, D. Esteve, F. Chiarello, A. Shnirman, Y. Makhlin, J. Schriefl, and G. Schön, Decoherence in a superconducting quantum bit circuit, Phys. Rev. B **72**, 134519 (2005).

[27] J. Braumüller, L. Ding, A. P. Vepsäläinen, Y. Sung, M. Kjaergaard, T. Menke, R. Winik, D. Kim, B. M. Niedzielski, A. Melville, J. L. Yoder, C. F. Hirjibehedin, T. P. Orlando, S. Gustavsson, and W. D. Oliver, Characterizing and Optimizing Qubit Coherence Based on Squid Geometry, Phys. Rev. Appl. **13**, 054079 (2020).

[28] R. W. Simmonds, K. M. Lang, D. A. Hite, S. Nam, D. P. Pappas, and J. M. Martinis, Decoherence in Josephson Phase Qubits from Junction Resonators, Phys. Rev. Lett. **93**, 077003 (2004).

[29] J. Eroms, L. C. van Schaarenburg, E. F. C. Driessen, J. H. Plantenberg, C. M. Huizinga, R. N. Schouten, A. H. Verbruggen, C. J. P. M. Harmans, and J. E. Mooij, Low-frequency noise in Josephson junctions for superconducting qubits, Appl. Phys. Lett. **89**, 122516 (2006).

[30] L. V. Abdurakhimov, I. Mahboob, H. Toida, K. Kakuyanagi, and S. Saito, A long-lived capacitively shunted flux qubit embedded in a 3d cavity, Appl. Phys. Lett. **115**, 262601 (2019).

[31] E. Albertinale, L. Balembois, E. Billaud, V. Ranjan, D. Flanigan, T. Schenkel, D. Estève, D. Vion, P. Bertet, and E. Flurin, Detecting spins by their fluorescence with a microwave photon counter, Nature **600**, 434 (2021).

[32] M. Bal, M. H. Ansari, J.-L. Orgiazzi, R. M. Lutchyn, and A. Lupascu, Dynamics of parametric fluctuations induced by quasiparticle tunneling in superconducting flux qubits, Phys. Rev. B **91**, 195434 (2015).

[33] I. Shani, E. G. Dalla Torre, and M. Stern, Coherence properties of a spin in a squeezed resonator, Phys. Rev. A **105**, 022617 (2022).